



Field-induced successive phase transitions in the J_1 - J_2 buckled honeycomb antiferromagnet $\text{Cs}_3\text{Fe}_2\text{Cl}_9$

Y. Ishii ¹, Y. Narumi,² Y. Matsushita,³ M. Oda,⁴ T. Kida ², M. Hagiwara,² and H. K. Yoshida⁴

¹*Department of Physics, Graduate School of Science, Hokkaido University, Sapporo 060-0810, Japan*

²*Center for Advanced High Magnetic Field Science, Graduate School of Science, Osaka University, Toyonaka, Osaka 560-0043, Japan*

³*National Institute for Materials Science, Tsukuba, Ibaraki 305-0044, Japan*

⁴*Department of Physics, Faculty of Science, Hokkaido University, Sapporo, Hokkaido 060-0810, Japan*



(Received 23 July 2020; revised 15 February 2021; accepted 17 February 2021; published 25 March 2021)

The magnetic properties of $\text{Cs}_3\text{Fe}_2\text{Cl}_9$ single crystals were investigated by magnetic and thermal measurements. The crystal structure of $\text{Cs}_3\text{Fe}_2\text{Cl}_9$ consists of a bilayer triangular lattice of Fe^{3+} ions. The analysis of magnetic susceptibility clarified that the intra- and interdimer interactions are comparable with each other, and $\text{Cs}_3\text{Fe}_2\text{Cl}_9$ is regarded as a spin-5/2 J_1 - J_2 buckled honeycomb antiferromagnet with the ferromagnetic interlayer interaction J_3 . The susceptibility for the magnetic field $H||c$ axis exhibits a sudden drop at the Néel temperature $T_N = 5.4$ K, indicating a first-order magnetic phase transition. One of the characteristic features is the linear temperature dependence below T_N . Furthermore, $\text{Cs}_3\text{Fe}_2\text{Cl}_9$ undergoes successive magnetic phase transitions in high magnetic fields along the c axis. We obtained a rich H - T phase diagram in which the $M_s/2$ magnetization-plateau phase is included. These unique magnetic behaviors probably originate from the competition of magnetic interactions and the easy-axis anisotropy in the antiferromagnetic J_1 - J_2 buckled honeycomb network.

DOI: [10.1103/PhysRevB.103.104433](https://doi.org/10.1103/PhysRevB.103.104433)

I. INTRODUCTION

Various nontrivial magnetic phenomena in systems with competing interactions, such as the triangular lattice, kagome, and J_1 - J_2 honeycomb networks, have been of significant interest for several decades, where J_1 and J_2 are the first and the second nearest neighbor interactions, respectively. In particular, the magnetism of quantum triangular lattice antiferromagnets (TLAFMs) has been intensively studied since the resonating valence bond state was predicted [1]. Although recent theoretical studies have reached the consensus that the ground state of quantum TLAFMs is a 120° spin-structure state with reduced moments instead of a spin liquid (SL) state [2–5], an additional competing interaction, such as a ring exchange interaction, may induce the SL state in quantum TLAFMs [6,7]. In fact, the observation of an SL state based on this mechanism was reported in the organic TLAFM compound κ -(ET) $_2\text{Cu}_2(\text{CN})_3$ [8,9]. On the other hand, in classical systems, various magnetic phenomena are expected to emerge, such as the Berezinskii-Kosterlitz-Thouless transition [10,11] and a chiral transition at finite temperature in XY systems [12].

Bilayer triangular lattice (BLTL) antiferromagnets also incorporate competing interactions in their crystal structures. In these structures, the BLTL layers are stacked along the c axis with $(1/3, 1/3)$ translation in the ab plane, where the three interactions J_1 , J_2 , and J_3 determine the magnetic network of the system, as shown in Fig. 1(a). When J_3 is much larger than the others, the magnetic network becomes a dimer-based system. In the opposite case, it is thought to be a J_1 - J_2 buckled honeycomb system coupled by J_3 . In this case, the inter-BLTL layer interactions J_1 become dominant (first

nearest neighbor) in the conventional honeycomb network, as shown in Fig. 1(b). Furthermore, the intratriangular lattice layer interactions J_2 can be regarded as the second nearest neighbor interactions of the honeycomb network, in which the J_2 competes with J_1 when being antiferromagnetic. In this case, the magnetism of the system can be regarded as J_1 - J_2 honeycomb antiferromagnet which is known as the frustrated spin system.

Actually, theoretical studies predict that the J_1 - J_2 Heisenberg classical honeycomb antiferromagnet (HAFM) shows a disordered magnetic ground state when $J_2/J_1 > 1/6$ [13,14], and experimental studies of $\text{Bi}_3\text{Mn}_4\text{O}_{12}(\text{NO}_3)$ with J_2/J_1 between 0.1 and 0.15 revealed an unusual ground state coming from the frustration by J_1 and J_2 [15–18].

Several compounds are known to be candidates for BLTL antiferromagnets. For example, $\text{Ba}_3\text{Mn}_2\text{O}_8$ (spin-1) is a dimer system with dominant antiferromagnetic (AF) J_3 , which shows a nonmagnetic spin singlet state [19–21]. In contrast, a buckled honeycomb magnetic network is realized in $\text{Ba}_2\text{NiTeO}_6$ (spin-1) with comparable AF J_1 and J_2 [22]. $\text{Ba}_2\text{NiTeO}_6$ shows a collinear stripe magnetic order with a propagation vector \mathbf{k}_{mag} of $(0, 1/2, 1)$ [23,24].

$A_3M_2X_9$ (A^+ = alkali metal, M^{3+} = transition metal, X^- = halogen) series compounds are also candidates for BLTLs. The crystal structure and exchange-interaction paths of J_1 , J_2 , and J_3 are shown in Figs. 2(a)–2(c). There are several compounds, such as spin-1/2 $\text{Cs}_3\text{Ti}_2\text{Cl}_9$ [25,26], spin-1 $\text{Cs}_3\text{V}_2\text{Cl}_9$ and $\text{Rb}_3\text{V}_2\text{Br}_9$ [27], and spin-3/2 $\text{Cs}_3\text{Cr}_2\text{Cl}_9$ and $\text{Cs}_3\text{Cr}_2\text{Br}_9$ [28,29]. Ti and Cr compounds can be regarded as dimer systems because of the strong J_3 , and they show a nonmagnetic ground state with a finite excitation gap. In particular, $\text{Cs}_3\text{Cr}_2\text{Cl}_9$ exhibits $M_s/3$ and $2M_s/3$ magnetization plateaus

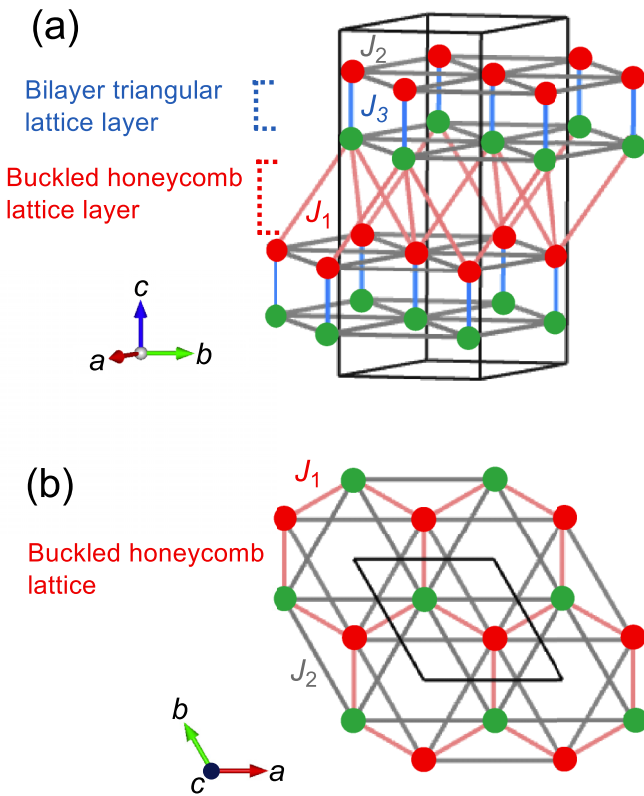


FIG. 1. (a) Schematic illustration of the bilayer triangular lattice. Red and green spheres represent magnetic ions. The interactions J_1 , J_2 , and J_3 are the interactions of the interbilayer triangular lattice plane, within the triangular lattice, and the intertriangular lattice within the bilayers, respectively. (b) Projection of the buckled honeycomb network onto the ab plane.

in a magnetic field because of the partially magnetized dimer (corresponding to the triplet excitation) [30].

Here, we focus on $\text{Cs}_3\text{Fe}_2\text{Cl}_9$ regarded as a classical spin-5/2 BLTL magnet. Previously, the temperature dependence of the magnetic susceptibility of a polycrystal sample was studied, and the formation of a nonmagnetic ground state with a small excitation gap was reported [31]. Micro-single-crystal synthesis by dehydration of concentrated hydrochloric acid aqueous solutions of cesium chloride and iron chloride was reported [32,33]. However, physical properties of single-crystal samples have not been reported so far. Recently, we succeeded in synthesizing single crystals of $\text{Cs}_3\text{Fe}_2\text{Cl}_9$ by applying the solvothermal method which enables us to grow large single crystals. In this paper, we report the synthesis, crystal structure, and magnetic properties of $\text{Cs}_3\text{Fe}_2\text{Cl}_9$, and we discuss various magnetic states realized in $\text{Cs}_3\text{Fe}_2\text{Cl}_9$ by comparing those with J_1 - J_2 buckled honeycomb antiferromagnets (BHAfMs).

II. EXPERIMENTS

Single crystals of $\text{Cs}_3\text{Fe}_2\text{Cl}_9$ were prepared by solvothermal synthesis. Stoichiometric mixtures of cesium chloride and iron chloride were placed in a Teflon-lined stainless steel autoclave with concentrated aqueous hydrochloric acid. The

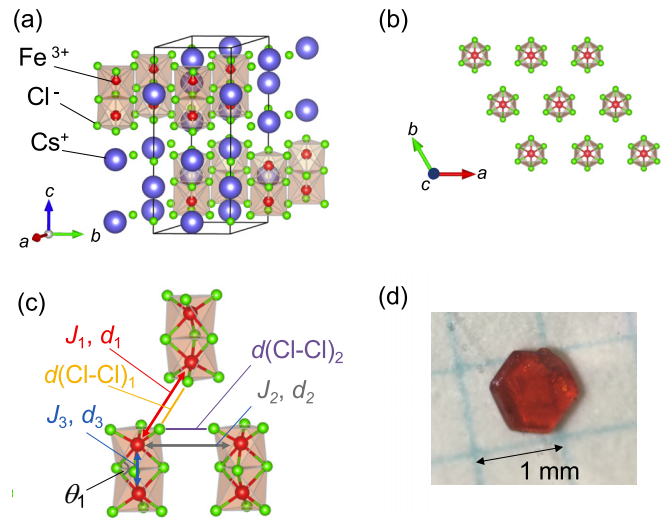


FIG. 2. (a) Perspective view of the crystal structure of $A_3M_2X_9$. (b) Triangular lattice plane made from the Fe_2Cl_9 dimer along the c direction. Cs ions are not shown for ease of viewing. (c) Three dominant interactions J_1 , J_2 , and J_3 corresponding to those of the bilayer triangular lattice shown in Fig. 1. The intradimer Fe-Fe distance d_3 , angle of intradimer Fe-Cl-Fe θ_1 , and interdimer Cl-Cl distances d_1 and d_2 are illustrated. (d) Photo of a single crystal of $\text{Cs}_3\text{Fe}_2\text{Cl}_9$.

autoclave was heated up to the temperature of 220°C and held at 220°C for 24 h, then slowly cooled down to room temperature which is approximately 25°C . Orange hexagonal plate crystals were obtained. The largest dimension is approximately 0.2 mm thick, with a diagonal length of approximately 1.0 mm, as shown in Fig. 2(d). As mentioned in Refs. [32,33], $\text{Cs}_3\text{Fe}_2\text{Cl}_9$ is slightly sensitive to air, and thus the crystal was dealt with in the argon-filled glove box to avoid air exposure. For the crystal structure analysis, a single hexagonal plate shaped crystal with dimensions of $0.094 \times 0.050 \times 0.032 \text{ mm}^3$ was selected. Data collection was carried out using Mo $K\alpha$ radiation ($\lambda = 0.71073 \text{ \AA}$) on a Rigaku AFC11 Saturn charge-coupled device (CCD) diffractometer with a VariMax confocal x-ray optics system. The sample temperature (113 K) was controlled by a flash-cooling stream system using N_2 gas. Cell refinement and data reduction were carried out using the D*TREK program package in the CRYSTALCLEAR software suite [34]. The structure was solved using SHELXT [35] and refined by full-matrix least squares on F^2 using SHELXL-2014 [35] in the WINGX program package [36]. Magnetic measurements of single-crystal $\text{Cs}_3\text{Fe}_2\text{Cl}_9$ were performed using a SQUID magnetometer (Quantum Design MPMS) up to 7 T. High-field magnetization measurements were carried out on aligned single crystals by the induction method in a pulsed high magnetic field of up to 25 T at the Center for Advanced High Magnetic Field Science at Osaka University. The absolute value of the high-field magnetization was calibrated with the magnetization measured with the SQUID magnetometer. Heat capacity measurements were performed on a single crystal by the relaxation method (Quantum Design PPMS) in magnetic fields of up to 13.5 T.

TABLE I. Refined structural parameters of Cs₃Fe₂Cl₉.

Atom	Wyckoff position	Occ.	<i>x</i>	<i>y</i>	<i>z</i>	<i>U</i> _{eq} (Å ²)
Cs1	2 <i>b</i>	1.0	0.0000	0.0000	0.2500	0.01067(6)
Cs2	4 <i>f</i>	1.0	0.3333	0.6667	0.41723(2)	0.01166(6)
Fe	4 <i>f</i>	1.0	0.6667	0.3333	0.34608(3)	0.00952(9)
Cl1	6 <i>h</i>	1.0	0.51618(6)	0.03235(12)	0.2500	0.01002(11)
Cl2	12 <i>k</i>	1.0	0.35031(9)	0.17516(4)	0.41052(3)	0.01156(9)

III. RESULTS

A. Crystal structure refinement

Single-crystal x-ray diffraction experiments on Cs₃Fe₂Cl₉ revealed that this compound crystallizes in a hexagonal system with the space group *P*6₃/*mmc* [*a* = 7.1898(3) Å and *c* = 17.6703(7) Å], and the final *R*1 value was 3.47%. The crystal structures of Cs₃Fe₂Cl₉ are illustrated in Figs. 2(a)–2(c), which are identical to those of the *A*₃*M*₂*X*₉ series of compounds. The structural parameters and details of the structural analysis are summarized in Table I and in Table S1 in the Supplemental Material [37], respectively. The selected bond distances *d*₁ (*J*₁ bond), *d*₂ (*J*₂ bond), *d*₃ (*J*₃ bond), *d*(Cl-Cl)₁ (the Cl-Cl distance between the TL planes), and *d*(Cl-Cl)₂ (the Cl-Cl distance within the TL planes), as well as the *M*-Cl-*M* angle θ_1 within the dimer, are summarized in Table II. Cs₃Fe₂Cl₉ has the longest *d*₃ length, and the shortest *d*₁, *d*₂, *d*(Cl-Cl)₁, and *d*(Cl-Cl)₂ in the Cs₃*M*₂Cl₉ family of compounds, which affects the magnetic properties of Cs₃Fe₂Cl₉.

B. Magnetic susceptibility

Figures 3(a) and 3(b) show the temperature dependence of the magnetic susceptibilities ($\chi = M/H$) for *H*||*c* axis (χ_c) and *H*||*ab* plane (χ_{ab}) at *H* = 1 T between 1.8 and 300 K, respectively. χ_c and χ_{ab} above 50 K can be fitted by the Curie-Weiss law. The Curie constant *C* = 4.52 and the Weiss temperature $\theta_W = -13.3$ K for the *H*||*c* axis, and *C* = 4.57 and $\theta_W = -16.0$ K for the *H*||*ab* plane were extracted from the fittings. The *g* values *g*_{*c*} = 2.03 and *g*_{*ab*} = 2.04 were evaluated from the Curie constants by assuming spin-5/2, and they are consistent with the results of X-band electron spin resonance (ESR) measurements, as presented in Figs. S1 and S2 in the Supplemental Material [37]. The negative θ_W indicates that the

net magnetic interaction is antiferromagnetic. We estimated the magnetic interactions *J*₁, *J*₂, and *J*₃ by high-temperature series expansion (HTSE) fitting [38] based on the following effective Hamiltonian:

$$\mathcal{H} = -J_1 \sum_{(i,j)_1} \mathbf{S}_i \cdot \mathbf{S}_j - J_2 \sum_{(i,j)_2} \mathbf{S}_i \cdot \mathbf{S}_j - J_3 \sum_{(i,j)_3} \mathbf{S}_i \cdot \mathbf{S}_j.$$

The χ_c and χ_{ab} were well reproduced with the parameter values of magnetic interactions *J*₁/*k*_B = -1.35 K (AF), *J*₂/*k*_B = -0.56 K (AF), and *J*₃/*k*_B = 2.95 K (F), as shown in Figs. 3(a) and 3(b). Here, the *g* values determined by the Curie-Weiss analyses were used in the HTSE fittings. The *J*₁, *J*₂, and *J*₃ values are comparable with each other, suggesting that Cs₃Fe₂Cl₉ is a model of the *J*₁-*J*₂ BHAFM with ferromagnetic *J*₃. Within the mean field theory, the calculated Weiss temperature $\theta_W = \sum z_i J_i S(S+1)/3k_B = 2.92(3J_1/k_B + 6J_2/k_B + J_3/k_B) = -13.1$ K, (where *z*_{*i*} is the coordination number of exchange interaction *J*_{*i*}, which is consistent with the experimental value. From the structural analysis, the Fe-Cl-Fe exchange bond angle of 84.35(3)° within the dimer is close to 90°. Thus, the exchange interaction is thought to be ferromagnetic or weak antiferromagnetic [39]. In addition, the Cl-Cl distances were shorter than those of other Cs₃*M*₂Cl₉ compounds, as shown in Table II. This situation causes three comparable interactions between *J*₁, *J*₂, and *J*₃ in Cs₃Fe₂Cl₉.

The temperature dependence of χ_c and χ_{ab} below 8 K at *H* = 1 T is presented in Fig. 4. χ_c drops steeply at *T*_N = 5.4 K, indicating the onset of an AF long-range order. The very sharp drops of χ_c suggest that the phase transition is first order. In addition, a linear temperature (linear *T*) dependence of the χ_c below *T*_N was observed. In contrast, χ_{ab} shows a subtle drop at *T*_N and temperature-independent behavior below *T*_N. These

TABLE II. The three *M*-*M* distances *d*₃, *d*₂, and *d*₁; the angles of *M*-*X*-*M* within the dimer (θ_1); the interdimer Cl-Cl distances within the plane [*d*(Cl-Cl)₁]; and the interdimer Cl-Cl distances between the planes [*d*(Cl-Cl)₂] in *A*₃*M*₂*X*₉ compounds from Refs. [25,27,28]. The data for Cs₃Fe₂Cl₉ were determined in this work.

	<i>d</i> ₁ (Å)	<i>d</i> ₂ (Å)	<i>d</i> ₃ (Å)
Cs ₃ Ti ₂ Cl ₉	7.1642(18)	7.3226(5)	3.215(3)
Cs ₃ V ₂ Cl ₉	7.162(3)	7.240(2)	3.1592(18)
Cs ₃ Cr ₂ Cl ₉	7.14(3)	7.217(2)	3.15(4)
Cs ₃ Fe ₂ Cl ₉	6.8426(9)	7.1898(4)	3.3955(1)
	θ_1 (deg)	<i>d</i> (Cl-Cl) ₁ (Å)	<i>d</i> (Cl-Cl) ₂ (Å)
Cs ₃ Ti ₂ Cl ₉	79.11(6)	3.9993(17)	3.8604(18)
Cs ₃ V ₂ Cl ₉	80.1(3)	3.973(10)	3.834(9)
Cs ₃ Cr ₂ Cl ₉	80.7(7)	4.035(7)	3.9167(11)
Cs ₃ Fe ₂ Cl ₉	84.35(3)	3.8416(8)	3.7780(3)

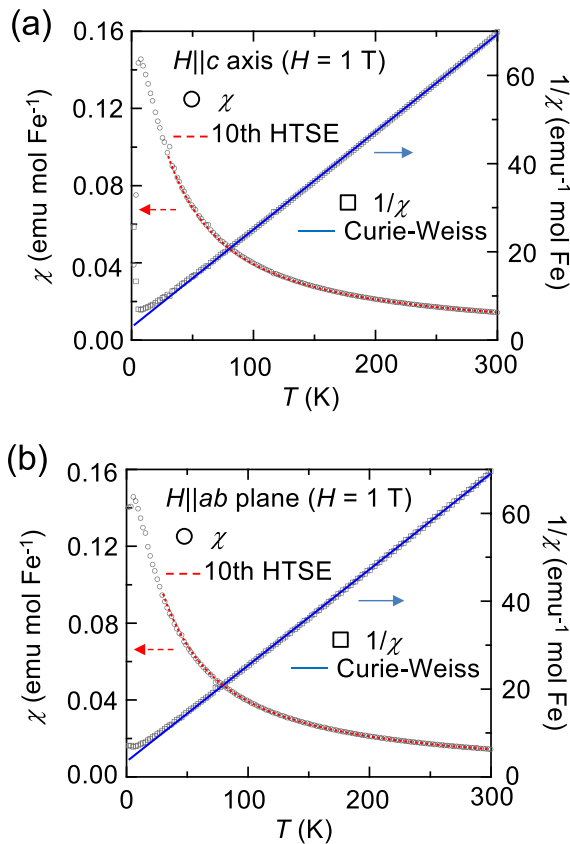


FIG. 3. Temperature dependence of magnetic susceptibilities of $\text{Cs}_3\text{Fe}_2\text{Cl}_9$ for $H \parallel c$ axis (a) and $H \parallel ab$ plane (b). Open circles (gray) and red broken lines represent the experimental results and the results of the tenth-order high-temperature expansion [38], respectively. Open squares (gray) and blue solid lines show the inverse susceptibilities and their Curie-Weiss fittings above 50 K, respectively.

results indicate that the ground state of $\text{Cs}_3\text{Fe}_2\text{Cl}_9$ is an AF ordered state with easy-axis anisotropy along the c axis.

The low-temperature χ_c in various magnetic fields below 8 K are shown in Fig. 5. As indicated by triangles,

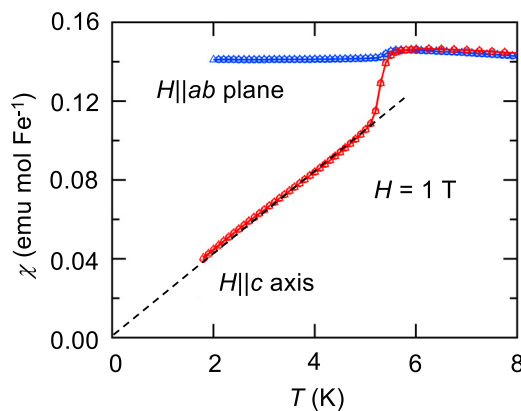


FIG. 4. Temperature dependence of magnetic susceptibilities for $H \parallel c$ axis and $H \parallel ab$ plane measured at 1 T. Dotted line for the $H \parallel c$ axis data is guide for the eyes for the linear T dependence of the susceptibility.

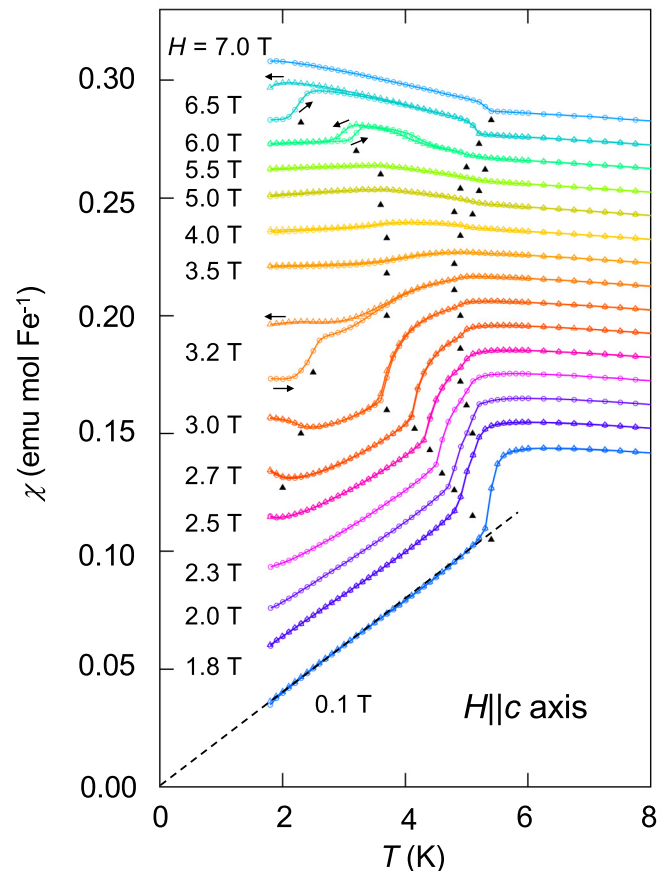


FIG. 5. Temperature dependence of magnetic susceptibilities in various magnetic fields below 8 K for $H \parallel c$ axis. For all plots, circles and triangles are the zero field cooling and field cooling data, respectively. Black solid triangles indicate the transition temperatures determined by the differentials of the magnetic susceptibilities (Fig. S4 in the Supplemental Material [37]) and the heat capacities. Data are shifted upward by 0.01 emu mol Fe^{-1} as an offset.

many magnetic phase transitions occur in magnetic fields, resulting in the production of a complicated magnetic field vs temperature phase diagram (these data are expanded in Fig. S3 [37]). The transition temperatures were determined from their temperature differentials $d\chi_c/dT$, shown in Fig. S4 [37], and the heat capacities will be displayed later in Fig. 9. In the low-field χ_c , the linear T behavior below T_N remains up to 2 T. The continuous temperature dependence of magnetic susceptibility may suggest that the directions of spin can change smoothly by the temperature changes. To our best knowledge, a few experimental observations of linear T magnetic susceptibilities have been reported in the spin-glass systems $\text{Fe}_{0.5}\text{Mn}_{0.5}\text{TiO}_3$ [40] and GdB_6 [41], and in the iron superconductors $\text{LaFeAsO}_{1-x}\text{F}_x$ [42,43]. In both systems, the predominant origin of the linear T behavior is thought to be magnetic frustration, which gives rise to innumerable degeneracy of metastable magnetic states causing the unique temperature dependences and the hysteretic magnetization process of $\text{Cs}_3\text{Fe}_2\text{Cl}_9$. The sharp drop gradually broadens as the magnetic field increases. This occurs because the transition splits into two, as confirmed by the heat capacity data. This split is prominent above 2.5 T. In addition, another

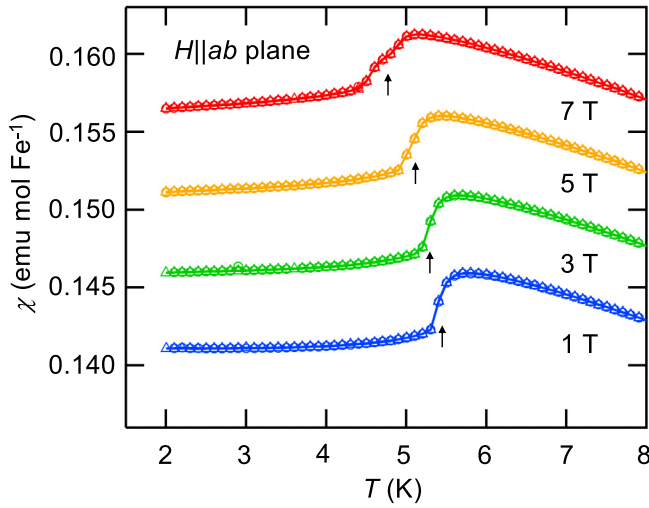


FIG. 6. Temperature dependence of magnetic susceptibilities at various magnetic fields below 8 K for $H||ab$ plane. For all plots, circles and triangles are the zero field cooling and field cooling data, respectively. Arrows indicate the transition temperatures. Data are shifted upward by $0.005 \text{ emu mol Fe}^{-1}$ as an offset.

anomaly appears at approximately 2 K at $H = 2.7 \text{ T}$; the temperature at the additional anomaly increases to 2.5 K at 3.2 T with hysteresis. Then, at 3.5 T, this lowest-temperature transition vanishes. At 4 T, the susceptibility begins to grow at the highest transition temperature of 5 K. Notably, the transition at 5 T splits into two transitions again at 5.1 and 4.7 K; this is confirmed by the $d\chi_c/dT$ (Fig. S4(d) [37]) and heat capacity data. These two peaks merge into a single peak at 6.5 T. The lowest transition at 6 T is accompanied by a hysteresis that becomes prominent at 6.5 T and probably moves to the temperature below 1.8 K at 7 T. The domain formation sometimes affects the physical properties at the first-order phase transition. The susceptibilities were only measured with warming after zero field cooling, followed by the field cooling process; the data were not taken in warming and cooling after the field-cooled process. Therefore, we cannot confirm whether there is an important effect of domain formation on the phase transitions in $\text{Cs}_3\text{Fe}_2\text{Cl}_9$ at this stage.

Figure 6 shows the temperature dependence of χ_{ab} upon heating up to 8 K in several magnetic fields. χ_{ab} shows one small transition, whose temperature decreases slightly with increasing field up to 7 T.

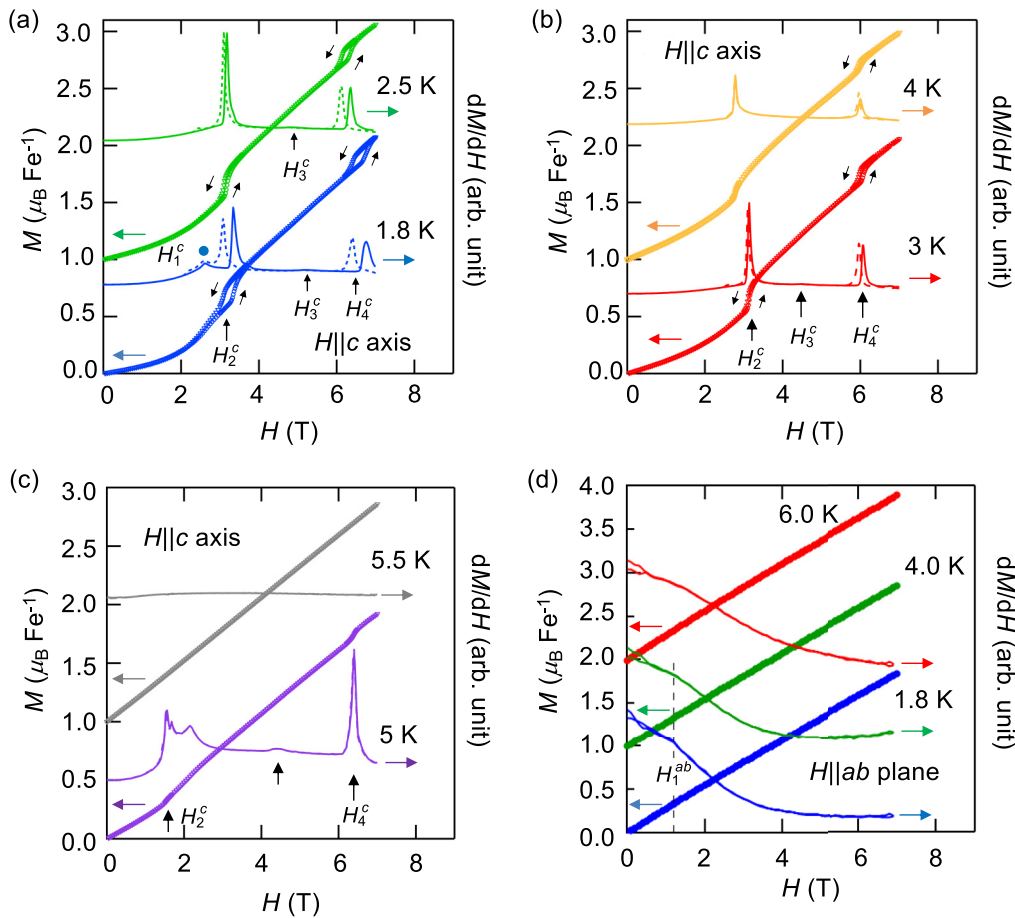


FIG. 7. [(a)–(c)] Magnetization curves (left axis) for the $H||c$ axis measured in magnetic fields of up to 7 T and field differentials dM/dH (right axis) with increasing and decreasing field. Solid lines and broken lines represent dM/dH with increasing and decreasing field, respectively. Data in [(a)–(c)] are shifted upward by $1.0 \mu_B \text{ Fe}^{-1}$ as an offset. Transition fields H_2^c and H_4^c were determined by taking the middle point of the hysteresis at each temperature. (d) Magnetization curves and dM/dH for the $H||ab$ plane measured in magnetic fields of up to 7 T. Data in (d) are also shifted upward by $1.0 \mu_B \text{ Fe}^{-1}$ as an offset.

C. Magnetization

Magnetization curves (M) and their field derivatives (dM/dH) in magnetic fields of up to 7 T at several temperatures for $H||c$ axis (M_c) and $H||ab$ plane (M_{ab}) are displayed in Figs. 7(a)–7(d) (dM/dH data for other temperatures are shown in Figs. S5(a) and S5(b) [37]). The M_c at $T = 1.8$ K shows a downward convex field dependence in the low magnetic field region and a tiny anomaly at $H_1^c = 2.6$ T, which is marked by a blue solid circle in the panel. Moreover, three successive transitions occur, at $H_2^c = 3.2$ T, $H_3^c = 5.2$ T, and $H_4^c = 6.6$ T. Two metamagnetic transitions at H_2^c and H_4^c are remarkable and accompanied by clear hysteresis. These hystereses indicate that the transitions are first order. The transitions at H_1^c and H_3^c are indiscernible above 2.5 and 4 K, respectively (enlarged dM/dH graphs around H_3^c are introduced in Fig. S6 [37]). The H_2^c and H_4^c slightly decrease with increasing temperature, and the widths of the hystereses at H_2^c and H_4^c become narrower than those at 1.8 K. Both hystereses vanish at 4 K. The transition at H_2^c splits into two, as seen in the double-peak structure of dM/dH at 5 K, and an additional broad peak appears at approximately 4.5 T indicated by the middle arrow. The M_c at 5.5 K shows a linear field dependence up to 7 T. In contrast, only one anomaly at $H_1^{ab} = 1.2$ T was observed for M_{ab} below T_N [Fig. 7(d)].

D. High-field magnetization

Figures 8(a) and 8(b) show the high-field M_c and M_{ab} up to 25 T at 1.4 K, respectively [the magnetization curves at other temperatures are shown in Figs. S7(a)–S7(f)]. The data include the field ascending (blue and green lines) and descending (red and orange lines) processes. M_c exhibits successive anomalies at H_2^c and H_4^c , which seem to be the same as those observed in the steady field M_c . The widths of the hystereses at H_2^c and H_4^c are larger than those measured in the steady field. This is caused by the sweep rate of the magnetic field in the nonequilibrium phenomenon of the first-order phase transition. Above the transition field at H_4^c , the $M_s/2$ magnetization plateau (M_s is the saturation magnetization) appears with a small finite slope up to $H_5^c = 11.3$ T. Then, a small anomaly around $H_6^c = 14.5$ T with small hysteresis was observed below the saturation field. Finally, M_c saturates at $H_s^c = 17.4$ T. It is noted that dM_c/dH above H_6^c gradually decreases with increasing magnetic field up to H_s^c .

M_{ab} shows a small anomaly with a hysteresis around $H_2^{ab} = 12.4$ T and saturates at $H_s^{ab} = 19.4$ T, which is larger than $H_s^c = 17.4$ T. dM_{ab}/dH is nearly constant below H_2^{ab} and shows a convex downward curve between H_2^{ab} and the saturation field. This behavior is largely different from that of dM_c/dH .

E. Heat capacity

The temperature dependence of the heat capacities (C_p) measured in various magnetic fields of up to 13.5 T for the $H||c$ axis is shown in Figs. 9(a)–9(c). Arrows in Figs. 9(a)–9(c) indicate the small peaks, which are enlarged in Fig. 9(d). Because of the unavailability of a nonmagnetic compound with the same crystal structure for the estimation of the lattice heat capacity, we plotted the total heat capacity data. In zero

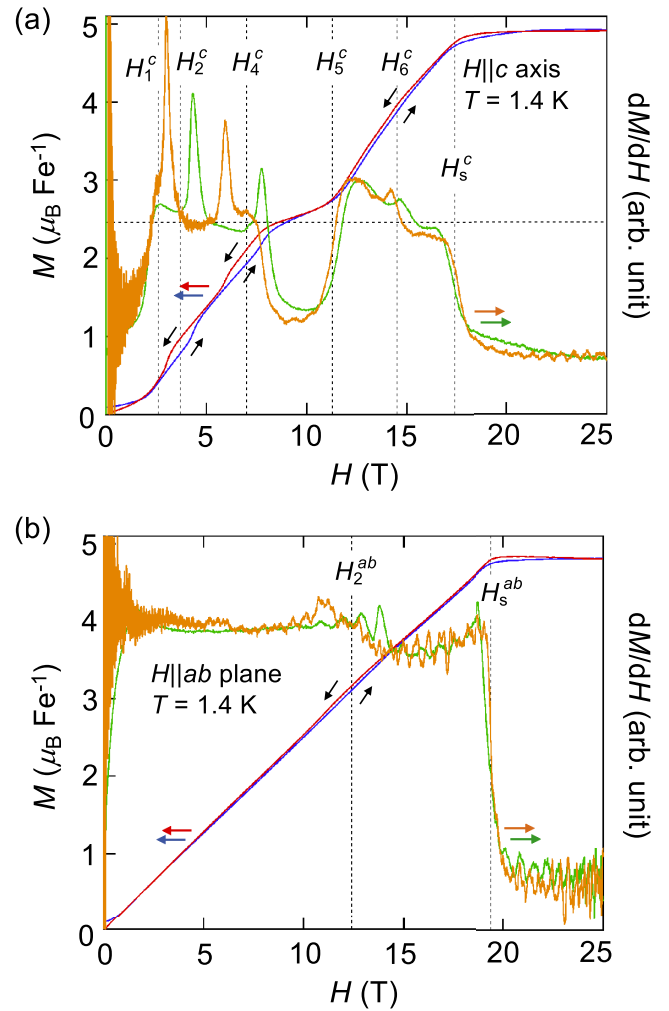


FIG. 8. High-field magnetization curves (blue and red lines) and field differentials dM/dH (green and orange lines) of $\text{Cs}_3\text{Fe}_2\text{Cl}_9$ for (a) the $H||c$ axis and (b) the $H||ab$ plane. Absolute values were calibrated using the steady field data measured by MPMS. Blue (green) and red (orange) lines are the data with increasing and decreasing field, respectively. Horizontal and vertical broken lines show $M_s/2$ and the transition fields, respectively. $H_1^c = 2.7$ T, $H_2^c = 3.7$ T, $H_4^c = 7$ T, $H_5^c = 11.3$ T, $H_6^c = 14.5$ T, $H_s^c = 17.4$ T, $H_2^{ab} = 12.4$ T, and $H_s^{ab} = 19.4$ T are estimated by taking the middle of the hysteresis at the transitions. The saturation magnetization value for the $H||c$ axis is $4.9 \mu_B \text{Fe}^{-1}$, and that for the $H||ab$ plane is $4.8 \mu_B \text{Fe}^{-1}$.

magnetic field, a single sharp peak was observed at 5.4 K. This suggests that the phase transition is first order, which is consistent with the steep drop in the low-field magnetic susceptibility at this temperature. The peak at 5.4 K gradually shifts to the lower-temperature side with increasing magnetic field, and splits into two sharp peaks at 2 T. The lower peak temperature is prominently influenced by the magnetic field, and it becomes λ shaped at 3.2 T. The higher one shows moderate field dependence and retains its peak shape. An additional peak appears at approximately 2 K at 2.8 T, which shifts to the higher-temperature side with increasing magnetic field and is missing in the 4 T data. The peak at 4.8 K in magnetic field at 4 T again splits into two steep peaks; the peaks merge into a single peak at 6.5 T. In contrast, the λ -

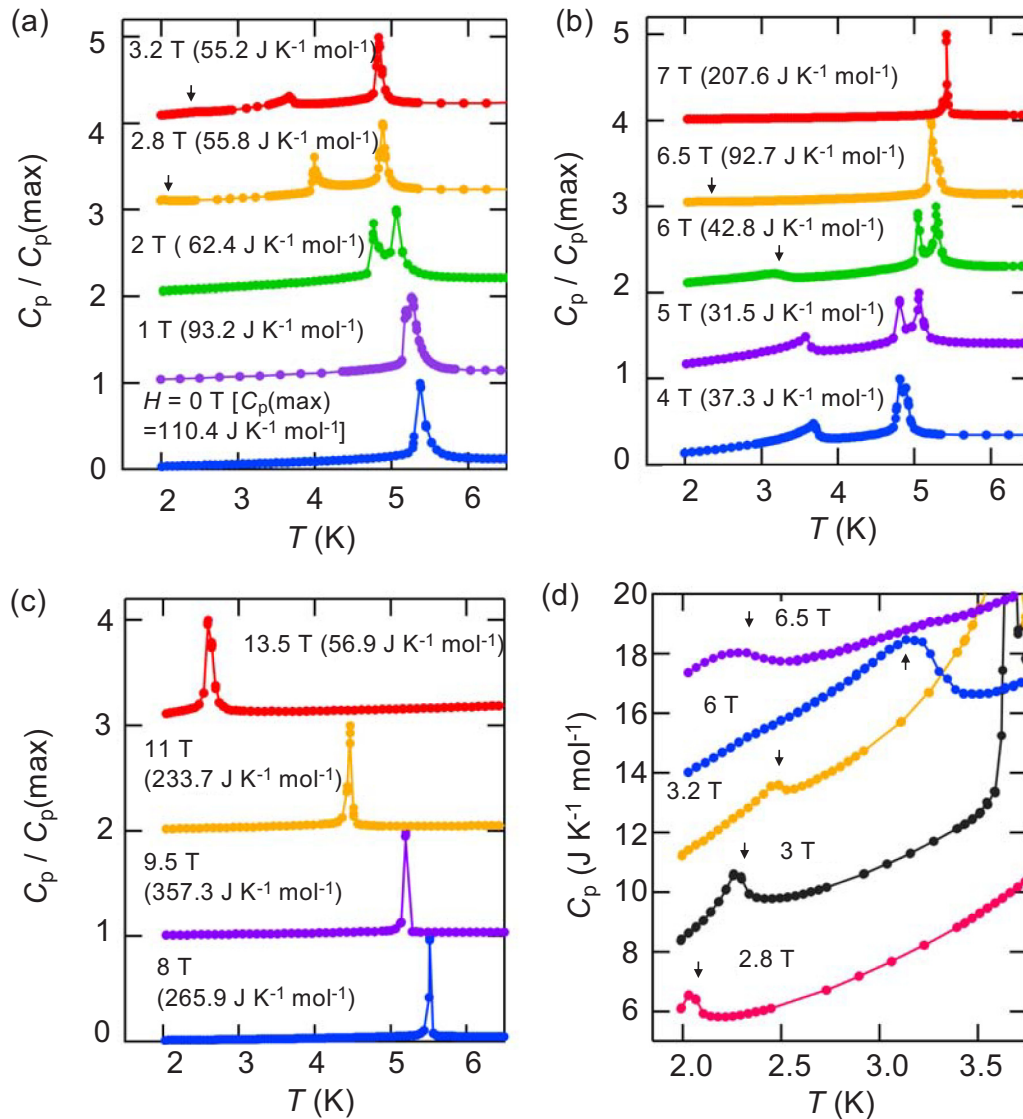


FIG. 9. [(a)–(c)] Heat capacities measured in various magnetic fields for the $H||c$ axis. Data are normalized by the largest peak top value $C_p(\max)$ for each data series shown in the graphs (value in parentheses). (d) Enlarged figure around small peaks in 2.8, 3, 3.2, 6, and 6.5 T. Data are shown with offset by 1.0 for [(a)–(c)], and by $3.0 \text{ J K}^{-1} \text{ mol}^{-1}$ for (d).

shape peak at 3.7 K in the magnetic field at 4 T moves to the lower-temperature side and disappears in the 7 T data. Above 7 T, only one sharp peak is observed, which corresponds to the first-order phase transition; the transition temperature shifts to the low-temperature side with increasing magnetic field. These results indicate that the phase transition from the high-temperature paramagnetic phase to the magnetic phase in an arbitrary magnetic field above 7 T up to 13.5 T is first order.

F. Phase diagram

The results of magnetic susceptibility, magnetization, and heat capacity measurements are summarized as the H - T magnetic phase diagrams for both the $H||c$ axis and $H||ab$ plane, as depicted in Figs. 10(a) and 10(b). When the transition is accompanied by hysteresis, the middle point of the hysteresis

is taken as the transition field, and the vertical bars represent the widths of the hysteresis field ranges. There are nine and three magnetic phases in the H - T phase diagram for the $H||c$ axis and $H||ab$ plane, respectively. The phase diagram for the $H||c$ axis is complicated. Almost all phase transitions have sharp anomalies or hysteresis, indicating first-order phase transitions. Only the transition from phase IV to phase V has a λ -type peak in the heat capacity; thus it should be the second-order phase transition.

IV. DISCUSSION

Bulk magnetization and heat capacity measurements revealed that $\text{Cs}_3\text{Fe}_2\text{Cl}_9$ was identified as a frustrated J_1 - J_2 buckled honeycomb antiferromagnet with ferromagnetic interlayer coupling, and established a magnetic ordered ground state (phase I) with the easy axis along the c axis. Because

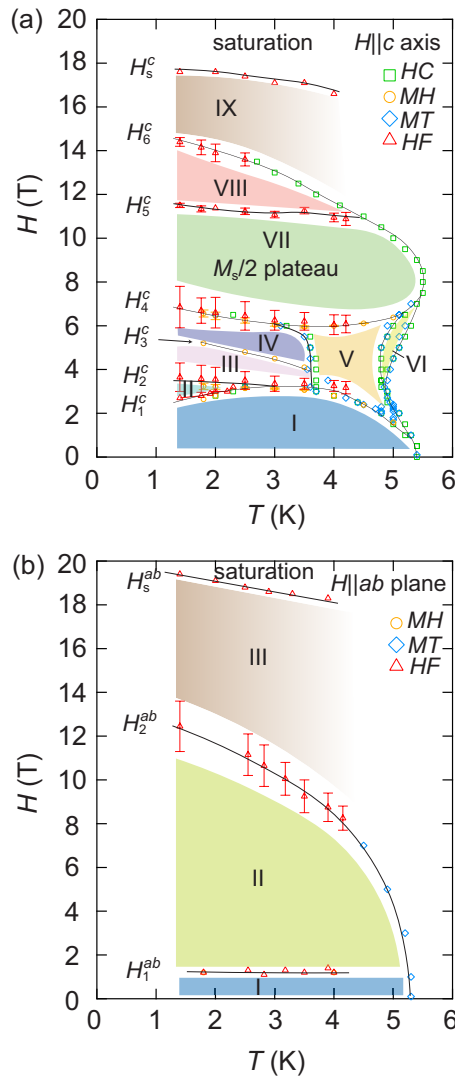


FIG. 10. Magnetic field vs temperature phase diagram for $\text{Cs}_3\text{Fe}_2\text{Cl}_9$ constructed by magnetic measurement, heat capacity measurement, and high-field magnetization data for (a) $H||c$ axis and for (b) $H||ab$ plane. Rhombic squares (blue), circles (orange), triangles (red), and squares (green) are the transition temperatures and fields determined from the temperature dependence of magnetic susceptibilities (MT), magnetization curves (MH), high-field magnetizations (HF), and heat capacities (HC), respectively. Bars represent the hysteresis field ranges of first-order phase transitions. Black lines are guides for the eye of phase boundaries.

the ferromagnetic J_3 cannot induce a magnetic frustration, it is reasonable to consider that the complicated magnetism observed in $\text{Cs}_3\text{Fe}_2\text{Cl}_9$ is attributed to the magnetic frustration in a two-dimensional J_1 - J_2 buckled honeycomb network. Therefore, we discuss the spin states of $\text{Cs}_3\text{Fe}_2\text{Cl}_9$ by comparing the obtained magnetic phase diagram with the theoretical phase diagram of the Ising J_1 - J_2 HAFM, which can be a clue for understanding the magnetic properties of the compound. Figure 11(a) shows the h/J_1 - J_2/J_1 phase diagram for the spin-5/2 Ising J_1 - J_2 HAFM at $T = 0$, which is calculated based on Ref. [44]. The candidate magnetic structures for the antiferromagnetic ordered state and $M_s/2$ plateau states

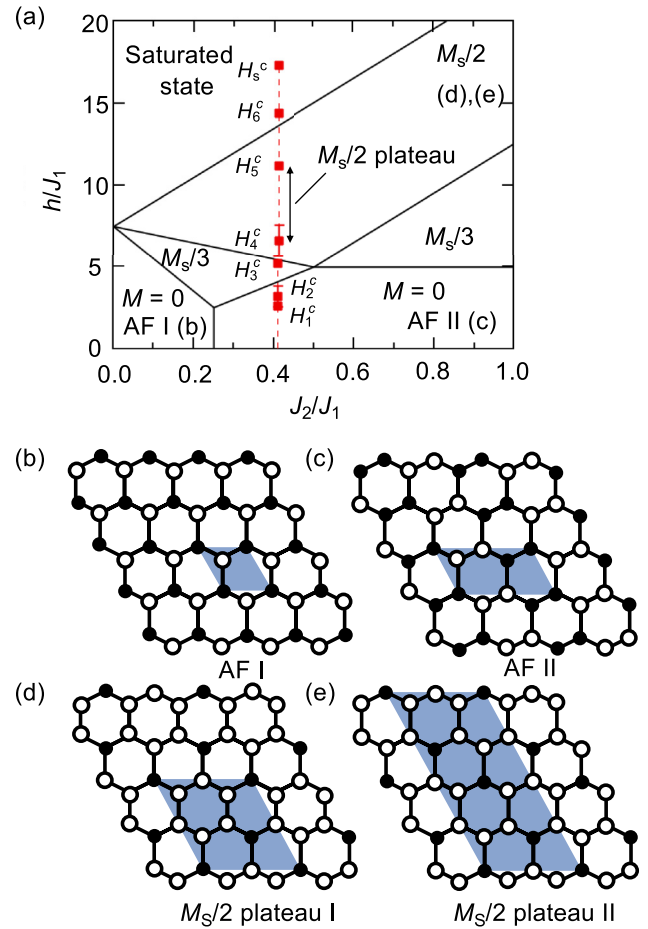


FIG. 11. (a) Ground state ($T = 0$) phase diagram for the $S = 5/2$ Ising J_1 - J_2 honeycomb antiferromagnet in a magnetic field, calculated in accordance with Ref. [44]. Critical fields determined from high-field magnetization curves at 1.4 K in $\text{Cs}_3\text{Fe}_2\text{Cl}_9$ normalized by the J_1 are plotted at the $J_2/J_1 = 0.41$ vertical line. Bars on the square marker represent the width of hysteresis of high-field magnetizations (hystereses of H_1^c , H_3^c , H_5^c , H_6^c , and H_s^c are smaller than the marker size). (b,c) Candidates for the ground state spin structures of Ising J_1 - J_2 HLAFM. In the present system, $\text{Cs}_3\text{Fe}_2\text{Cl}_9$, AF II is expected to be the ground state with $J_2/J_1 = 0.41$ (see text). [(d),(e)] Candidates for the $M_s/2$ plateau of the J_1 - J_2 HLAFM model. Open and closed circles represent up and down spins, respectively. Blue shaded regions in [(b)–(e)] correspond to the magnetic unit cell.

are illustrated in Figs. 11(b)–11(e). In the theoretical phase diagram, the $M_s/3$ and $M_s/2$ plateaus are stabilized in a wide area, except for $J_2/J_1 = 0$ and 0.5; the $M_s/3$ plateau disappears at $J_2/J_1 = 0.5$, and both $M_s/3$ and $M_s/2$ plateaus vanish at $J_2/J_1 = 0$. The magnetization curve for the system with $J_2/J_1 \neq 0, 0.5$ should exhibit a stepwise behavior from the AF phase to the $M_s/3$ plateau, via the $M_s/2$ plateau, and the saturated state, as observed in the Ising-like J_1 - J_2 BHAFM $\text{Ba}_2\text{CoTeO}_6$ [44].

From the magnetic susceptibility measurements, the ratio of interactions of $\text{Cs}_3\text{Fe}_2\text{Cl}_9$ is expected to be $J_2/J_1 = 0.41$. The critical fields of successive phase transitions in $\text{Cs}_3\text{Fe}_2\text{Cl}_9$ determined from the high-field magnetization at

1.4 K are plotted along the $J_2/J_1 = 0.41$ line in Fig. 11(a). The phase boundaries of the $M_s/2$ plateau, a region between H_4^c and H_5^c , are close to the calculated boundaries of the Ising J_1 - J_2 HAFM; however, there are clear discrepancies between the theoretical and experimental phase boundaries. In particular, a prominent difference is that there is no $M_s/3$ plateau in $\text{Cs}_3\text{Fe}_2\text{Cl}_9$, but one interesting issue to be noted is that the magnetization value at $H = (H_2^c + H_4^c)/2 = 5.4$ T is approximately one-third of M_s . An explanation of all the observed magnetic phases is beyond this simple Ising model calculation. These discrepancies probably originate from the competition of magnetic interactions and the easy-axis anisotropy, which give rise to long-range collinear spin arrangements and noncollinear multiple- q states, as discussed later.

Here, we focus on the spin arrangements of the ground state and the $M_s/2$ plateau phase compared with the theoretical calculations. First, we consider phase I as the ground state phase of $\text{Cs}_3\text{Fe}_2\text{Cl}_9$, compared with the AF I and AF II in Figs. 11(b) and 11(c); the Néel-type AF I [Fig. 11(b)] and the stripe AF II [Fig. 11(c)] are expected in the theoretical h/J_1 - J_2/J_1 phase diagram [44]. The energies for one magnetic ion with spin-5/2 in the AF I and AF II spin structures are described as $E_I = -75J_1/8 + 75J_2/4$ and $E_{II} = -25J_1/8 - 25J_2/4$, respectively. The AF II structure is stabilized as a zero-field ground state when $E_I > E_{II}$, which corresponds to the situation where $J_2/J_1 > 0.25$. Thus, the AF II structure is plausible for the ground state of $\text{Cs}_3\text{Fe}_2\text{Cl}_9$ because the experimental ratio $J_2/J_1 = 0.41$ is larger than 0.25. Next, the observed $M_s/2$ plateau phase is compared with $M_s/2$ plateaus I and II, as shown in Figs. 11(d) and 11(e). The plateau I and II structures are the expected models of the $M_s/2$ plateau, but the energies of both spin structures are degenerate for arbitrary J_2/J_1 ; the calculated energy is $E(M_s/2)_I = E(M_s/2)_{II} = 0$ only when the exchange interaction is taken into account. Therefore, we are not able to distinguish the spin structures realized in phase VII of $\text{Cs}_3\text{Fe}_2\text{Cl}_9$; more analyses and experiments are required to obtain further insight into the magnetic structure. As seen in the phase diagram of $\text{Cs}_3\text{Fe}_2\text{Cl}_9$, the boundary of the $M_s/2$ plateau phase protrudes to the higher-temperature side. This suggests that the thermal fluctuation may contribute to the stability of the $M_s/2$ plateau. Possibly this phenomenon is related to the thermal order by disorder effect which is pointed out in the kagome antiferromagnet [45]. Because there has been no theoretical study of the detailed thermal effect on the magnetization, it is necessary to discuss the thermal effect on $\text{Cs}_3\text{Fe}_2\text{Cl}_9$ quantitatively.

One of the features of the experimental phase diagram is its complexity compared with the theoretical one; thus an interesting state may exist in the complicated phase diagram of $\text{Cs}_3\text{Fe}_2\text{Cl}_9$. Recently, Shimokawa and Kawamura predicted that the multiple- q state could emerge in Heisenberg J_1 - J_2 HAFMs [46]. They calculated that the multiple- q state was stabilized at the finite temperature (finite- T) and finite magnetic field (finite- H) region for $J_2/J_1 = 0.18$. Multiple- q states are also expected to be realized in frustrated systems such as J_1 - J_2 (J_1 - J_3) TLAfMs in finite- T and finite- H regions [47]. Experimental investigations have suggested that a possible multiple- q state can be realized in spin-3/2 J_1 - J_2

HAFM $\text{Bi}_3\text{Mn}_4\text{O}_{12}(\text{NO}_3)$ [46]. In $\text{Cs}_3\text{Fe}_2\text{Cl}_9$, J_2/J_1 is different from that in Ref. [46]; therefore the values cannot be simply compared with each other, but we speculate that there are multiple- q states in the phase diagram of $\text{Cs}_3\text{Fe}_2\text{Cl}_9$ at finite temperature. In particular, it can be expected that phases V and VI stabilized at finite T and finite H are candidates for the multiple- q state. These phases will be of interest in $\text{Cs}_3\text{Fe}_2\text{Cl}_9$ and should be investigated in future studies, such as neutron diffraction experiments in magnetic fields.

Anisotropy plays a significant role in the magnetic properties of this frustrated compound. Here, we discuss the origin of the magnetic anisotropy in $\text{Cs}_3\text{Fe}_2\text{Cl}_9$ with the $3d^5$ electron configuration of the Fe^{3+} ion. In general, it is expected that the $3d^5$ ion leads to an isotropic Heisenberg system because the orbital angular momentum L is zero in a moderate ligand field electron (Hund's rule). However, there is a magnetic anisotropy observed in some materials with the $3d^5$ electron configuration. For example, the single-ion anisotropy was discussed in the spin-5/2 TLAfM $\text{RbFe}(\text{MoO}_4)_2$ [48] and the multiferroic material CuFeO_2 [49]. Particularly, the emergence of Ising anisotropy according to the finite orbital momentum of the Fe^{4+} ion coming from the charge transfer was elucidated in CuFeO_2 . Otherwise, the dipolar interaction gives rise to a magnetic anisotropy as observed in MnF_2 [50]. Here, we consider the single-ion anisotropy and the dipolar interaction for $\text{Cs}_3\text{Fe}_2\text{Cl}_9$. First, the single-ion anisotropy can modulate the Weiss temperatures for the $H||c$ axis and $H||ab$ plane, and the relationship between them is given as

$$\theta_W(c) - \theta_W(ab) = \left(\frac{D}{k_B}\right) \frac{(2S-1)(2S+3)}{10},$$

where $\theta_W(c)$, $\theta_W(ab)$, D , k_B , and S are the Weiss temperature for the $H||c$ axis, $H||ab$ plane, the coefficient of single-ion anisotropy (which is included as $-DS_z^2$ in the Hamiltonian), Boltzmann constant, and spin quantum number, respectively [51]. This formula allows us to estimate the coefficient of single-ion anisotropy as $(D/k_B) = 0.84$ K, resulting in the Ising anisotropy of $\text{Cs}_3\text{Fe}_2\text{Cl}_9$, though the precise origin has not been clarified. Next, we consider the dipolar interaction which induces a finite anisotropy in orbital quenched antiferromagnets with an ordered magnetic structure. When the ground state is the AF II state, the anisotropy becomes an easy-axis type within the third nearest neighbor interactions as shown in Figs. S10(a)–S10(d) in the Supplemental Material [37]. The energy of the easy-axis structure is -0.42 K. The anisotropy field (H_a) was estimated by $H_a = (H_s^{ab} - H_s^c)/2 = 1.0$ T (1.3 K). The energy scale agrees well with the sum of the single-ion anisotropy and the dipolar interaction. Therefore, we conclude that the anisotropy of $\text{Cs}_3\text{Fe}_2\text{Cl}_9$ comes from the single-ion anisotropy and the dipolar interaction.

V. CONCLUSION

We succeeded in synthesizing single crystals of $\text{Cs}_3\text{Fe}_2\text{Cl}_9$ and investigated the crystal structure and magnetic properties of these single crystals. $\text{Cs}_3\text{Fe}_2\text{Cl}_9$ has competing magnetic interactions $J_1/k_B = -1.35$ K, $J_2/k_B = -0.56$ K, and $J_3/k_B = 2.95$ K. This compound exhibits a rich phase diagram, including the $M_s/2$ magnetization plateau for the $H||c$ axis. The competition between the first- and second-order

phase transitions is also of significant interest in this system. We conclude that the complicated H - T phase diagram was realized by the competition of easy-axis anisotropy and antiferromagnetic J_1 and J_2 with a buckled honeycomb network, which is a unique system in the $A_3M_2X_9$ series of compounds. To determine the magnetic structures in the remaining magnetic phases and obtain a qualitative understanding of the magnetism of the J_1 - J_2 BHAFM, x-ray diffraction, DFT calculation, neutron diffraction, and NMR experiments in high magnetic fields are required.

ACKNOWLEDGMENTS

We thank T. Masuda, M. Hagihala, A. Matsumoto, R. Tomaru, T. Kimura, and T. Matsumoto for fruitful discussions. This work was supported by JSPS KAKENHI Grants No. 15K05155, No. 15K17686, No. 18K03529, No. 17H06137, No. 17K18758, and No. 19J14391. This work was partly carried out at the Center for Advanced High Magnetic Field Science at Osaka University under the Visiting Researcher's Program of the Institute for Solid State Physics, the University of Tokyo.

-
- [1] P. W. Anderson, *Mater. Res. Bull.* **8**, 153 (1973).
 [2] D. A. Huse and V. Elser, *Phys. Rev. Lett.* **60**, 2531 (1988).
 [3] Th. Jolicœur and J. C. Le Guillou, *Phys. Rev. B* **40**, 2727 (1989).
 [4] B. Bernu, P. Lecheminant, C. Lhuillier, and L. Pierre, *Phys. Rev. B* **50**, 10048 (1994).
 [5] S. R. White and A. L. Chernyshev, *Phys. Rev. Lett.* **99**, 127004 (2007).
 [6] G. Misguich, C. Lhuillier, B. Bernu, and C. Waldtmann, *Phys. Rev. B* **60**, 1064 (1999).
 [7] W. LiMing, G. Misguich, P. Sindzingre, and C. Lhuillier, *Phys. Rev. B* **62**, 6372 (2000).
 [8] Y. Shimizu, K. Miyagawa, K. Kanoda, M. Maesato, and G. Saito, *Phys. Rev. Lett.* **91**, 107001 (2003).
 [9] O. I. Motrunich, *Phys. Rev. B* **72**, 045105 (2005).
 [10] Z. L. Berezinskii, *Zh. Eksp. Teor. Fiz.* **61**, 1144 (1971) [*Sov. Phys.-JETP* **34**, 610 (1971)].
 [11] J. M. Kosterlitz and D. J. Thouless, *J. Phys. C* **6**, 1181 (1973).
 [12] S. Miyashita and H. Shiba, *J. Phys. Soc. Jpn.* **53**, 1145 (1984).
 [13] E. Rastelli, A. Tassi, and L. Reatto, *Physica B+C (Amsterdam)* **97**, 1 (1979).
 [14] S. Katsura, T. Ide, and T. Morita, *J. Stat. Phys.* **42**, 381 (1986).
 [15] O. Smirnova, M. Azuma, N. Kumada, Y. Kusano, M. Matsuda, Y. Shimakawa, T. Takei, Y. Yonesaki, and N. Kinomura, *J. Am. Chem. Soc.* **131**, 8313 (2009).
 [16] M. Matsuda, M. Azuma, M. Tokunaga, Y. Shimakawa, and N. Kumada, *Phys. Rev. Lett.* **105**, 187201 (2010).
 [17] N. Onishi, K. Oka, M. Azuma, Y. Shimakawa, Y. Motome, T. Taniguchi, M. Hiraishi, M. Miyazaki, T. Masuda, A. Koda, K. M. Kojima, and R. Kadono, *Phys. Rev. B* **85**, 184412 (2012).
 [18] S. Okubo, T. Ueda, H. Ohta, W. Zhang, T. Sakurai, N. Onishi, M. Azuma, Y. Shimakawa, H. Nakano, and T. Sakai, *Phys. Rev. B* **86**, 140401(R) (2012).
 [19] M. Uchida, H. Tanaka, M. I. Bartashevich, and T. Goto, *J. Phys. Soc. Jpn.* **70**, 1790 (2001).
 [20] M. Uchida, H. Tanaka, H. Mitamura, F. Ishikawa, and T. Goto, *Phys. Rev. B* **66**, 054429 (2002).
 [21] H. Tsujii, B. Andracka, M. Uchida, H. Tanaka, and Y. Takano, *Phys. Rev. B* **72**, 214434 (2005).
 [22] V. P. Köhl, U. Müller, and D. Reinen, *Z. Anorg. Allg. Chem.* **392**, 124 (1972).
 [23] S. Asai, M. Soda, K. Kasatani, T. Ono, M. Avdeev, and T. Masuda, *Phys. Rev. B* **93**, 024412 (2016).
 [24] S. Asai, M. Soda, K. Kasatani, T. Ono, V. O. Garlea, B. Winn, and T. Masuda, *Phys. Rev. B* **96**, 104414 (2017).
 [25] T. Gloger, D. Hinz, G. Meyer, and A. Lachgar, *Z. Kristallogr.* **211**, 821 (1996).
 [26] B. Leuenberger, H. U. Güdel, and A. Furrer, *Chem. Phys. Lett.* **126**, 255 (1986).
 [27] B. Leuenberger, B. Briat, J. C. Canit, A. Furrer, P. Fischer, and H. U. Güdel, *Inorg. Chem.* **25**, 2930 (1986).
 [28] B. Leuenberger, H. U. Güdel, and P. Fischer, *J. Solid State Chem.* **64**, 90 (1986).
 [29] B. Leuenberger, H. U. Güdel, J. K. Kjems, and D. Petitgrand, *Inorg. Chem.* **24**, 1035 (1985).
 [30] T. Ziman, J. P. Boucher, Y. Inagaki, and Y. Ajiro, *J. Phys. Soc. Jpn.* **74**, 119 (2005).
 [31] A. P. Ginsberg and M. B. Robin, *Inorg. Chem.* **2**, 817 (1963).
 [32] H. Yamatera and K. Nakatsu, *Bull. Chem. Soc. Jpn.* **27**, 244 (1954).
 [33] M. T. Kovsarnechan, J. Roziere, and D. Mascherpa-Corral, *J. Inorg. Nucl. Chem.* **40**, 2009 (1976).
 [34] *CRYSTALCLEAR* (Rigaku Corporation, Tokyo, Japan, 2005).
 [35] G. M. Sheldrick, *Acta Crystallogr., Sect. A* **71**, 3 (2015).
 [36] L. J. Farrugia, *J. Appl. Crystallogr.* **32**, 837 (1999).
 [37] See Supplemental Material at <http://link.aps.org/supplemental/10.1103/PhysRevB.103.104433> for the details of experimental data and calculations which are not introduced in the main text.
 [38] A. Lohmann, H.-J. Schmidt, and J. Richter, *Phys. Rev. B* **89**, 014415 (2014).
 [39] J. Kanamori, *J. Phys. Chem. Solids* **10**, 87 (1959).
 [40] A. Ito, H. Aruga, E. Trikai, M. Kikuchi, Y. Syono, and H. Takei, *Phys. Rev. Lett.* **57**, 483 (1986).
 [41] A. V. Semeno, M. A. Anisimov, A. V. Bogach, S. V. Demishev, M. I. Gilmanov, V. B. Filipov, N. Yu. Shitsevalova, and V. V. Glushkov, *Sci. Rep.* **10**, 18214 (2020).
 [42] R. Klingeler, N. Leps, I. Hellmann, A. Popa, U. Stockert, C. Hess, V. Kataev, H.-J. Grafe, F. Hammerath, G. Lang, S. Wurmehl, G. Behr, L. Harnagea, S. Singh, and B. Büchner, *Phys. Rev. B* **81**, 024506 (2010).
 [43] G. M. Zhang, Y. H. Su, Z. Y. Lu, Z. Y. Weng, D. H. Lee, and T. Xiang, *Europhys. Lett.* **86**, 37006 (2009).
 [44] P. Chanlert, N. Kurita, H. Tanaka, D. Goto, A. Matsuo, and K. Kindo, *Phys. Rev. B* **93**, 094420 (2016).
 [45] M. E. Zhitomirsky, *Phys. Rev. Lett.* **88**, 057204 (2002).
 [46] T. Shimokawa and H. Kawamura, *Phys. Rev. Lett.* **123**, 057202 (2019).
 [47] T. Okubo, S. Chung, and H. Kawamura, *Phys. Rev. Lett.* **108**, 017206 (2012).

- [48] S. A. Klimin, M. N. Popova, B. N. Mavrin, P. H. M. van Loosdrecht, L. E. Svistov, A. I. Smirnov, L. A. Prozorova, H.-A. Krug von Nidda, Z. Seidov, A. Loidl, A. Ya. Shapiro, and L. N. Demianets, *Phys. Rev. B* **68**, 174408 (2003).
- [49] Y. Narumi, T. Nakamura, H. Ikeno, N. Terada, T. Morioka, K. Saito, H. Kitazawa, K. Kindo, and H. Nojiri, *J. Phys. Soc. Jpn.* **85**, 114705 (2016).
- [50] F. Keffer, *Phys. Rev.* **87**, 608 (1952).
- [51] D. C. Johnston, *Phys. Rev. B* **95**, 094421 (2017).